AGU PUBLICATIONS

Tectonics

RESEARCH ARTICLE
10.1002/2015TC003908

Key Points:
- We model flat-slab subduction in southwestern Mexico along the MASE transect
- The flat slab induces 1 km of fore-arc subsidence and a neutral stress state
- Relatively high gravitational potential energy causes extension in the TMVB

Supporting Information:
- Text S1 and Figures S1–S9

Correspondence to:
M. Gérault,
melanie.gerault@univ-lyon1.fr

Citation:
Gérault, M., L. Husson, M. S. Miller, and E. D. Humphreys (2015), Flat-slab subduction, topography, and mantle dynamics in southwestern Mexico, *Tectonics*, *34*, 1892–1909, doi:10.1002/2015TC003908.

Received 15 APR 2015
Accepted 21 JUL 2015
Accepted article online 27 JUL 2015
Published online 23 SEP 2015

Flat-slab subduction, topography, and mantle dynamics in southwestern Mexico

Mélanie Gérault[1,2], Laurent Husson[3], Meghan S. Miller[1], and Eugene D. Humphreys[4]

[1]Department of Earth Sciences, University of Southern California, Los Angeles, California, USA, [2]Now at Laboratoire de Sciences de la Terre UMR 5570, Université Lyon 1, Lyon, France, [3]ISTerre, UMR CNRS 5275, Joseph Fourier University, Grenoble, France, [4]Department of Geological Sciences, University of Oregon, Eugene, Oregon, USA

Abstract Topography above subduction zones arises from the isostatic contribution of crustal and lithospheric buoyancy, as well as the dynamic contribution from slab-driven mantle flow. We evaluate those effects in southwestern Mexico, where a segment of the Cocos slab subducts horizontally. The eastern part of the volcanic arc—the Trans-Mexican Volcanic Belt—stands at an average elevation of 2.3 km, nearly 1.3 km above the fore-arc. Lateral changes in bulk crustal density are relatively small, and seismic imaging shows that there is little variation in crustal thickness between these two regions. Thus, the elevation difference between the arc and the fore-arc should arise from differences in mantle properties. We present finite element models of flat-slab subduction that provide a simultaneous match to topography, plate velocities, and stress state in the overriding plate. We find that the dynamic effects are primarily controlled by the amount of coupling at the subduction interface and in the mantle wedge, the lack of slab anchoring into the lower mantle, and the absence of continental mantle lithosphere. With a mantle wedge and a subduction interface that are, respectively, 2 and 4 orders of magnitude weaker than the asthenosphere, the flat slab exerts a downward pull that can explain most of the elevation difference between the fore-arc and the arc. We infer that lateral viscosity variations play a significant role in shaping dynamic topography in complex tectonic settings and that sublithospheric dynamics can influence the topography at wavelengths that are significantly shorter than previously recognized.

1. Introduction

The topography of the Earth reflects the density structure of the tectonic plates and the underlying mantle. Mass anomalies at crustal and lithospheric depths are balanced by variations in surface elevation that can remain stable over long timescales. This is typically referred to as the isostatic topography. Mass anomalies at greater depths belong to the convecting mantle and give rise to transient changes in surface elevation. This is typically referred to as dynamic topography. The role of mantle flow in the topography of both continental and oceanic regions is particularly significant in regions affected by a history of subduction, as inferred from geological and geophysical data [e.g., *Spencer*, 1996; *Guillaume et al.*, 2009; *Dávila et al.*, 2010; *Liu et al.*, 2011]. This has been discussed in a number of analytical, semi-analytical, and numerical modeling studies [e.g., *Mitrovica et al.*, 1989; *Gurnis*, 1990, 1993; *Zhong and Gurnis*, 1994; *Zhong and Davies*, 1999; *Billen and Gurnis*, 2001; *Husson*, 2006; *Zhang et al.*, 2012; *Dávila and Lithgow-Bertelloni*, 2013; *Faccenna et al.*, 2014; *Husson et al.*, 2014], as well as a few analog modeling studies [*Guillaume et al.*, 2010; *Husson et al.*, 2012]. However, it has been challenging to compare the results of theoretical models to the "observed" dynamic topography because, as a model itself, it can be limited by uncertainties in the thermochemical structure of the lithosphere [e.g., *Lithgow-Bertelloni and Gurnis*, 1997; *Steinberger*, 2007; *Conrad and Husson*, 2009; *Flament et al.*, 2013]. One way of minimizing this issue is to focus on an area where local geophysical studies have allowed a better structural constraint of the lithosphere and underlying mantle. Building upon recent, higher-resolution seismic images of southwestern Mexico, this study aims at understanding the role of the flat Cocos slab and the asthenospheric mantle versus that of the overriding plate in controlling the local topography. We also aim at understanding the role that lateral viscosity variations (LVVs) have on dynamic topography. To some extent, long-wavelength topography can be modeled with a simple 1-D treatment of the rheology (e.g., see reviews by *Dávila and Lithgow-Bertelloni* [2013] and *Flament et al.* [2013]). However, *Kaban et al.* [2014] recently demonstrated the significant effect that lateral viscosity variations (LVVs) have on dynamic topography at plate boundaries, and the role of LVVs in various aspects of subduction dynamics has long been recognized [e.g., *Zhong and Gurnis*, 1994;

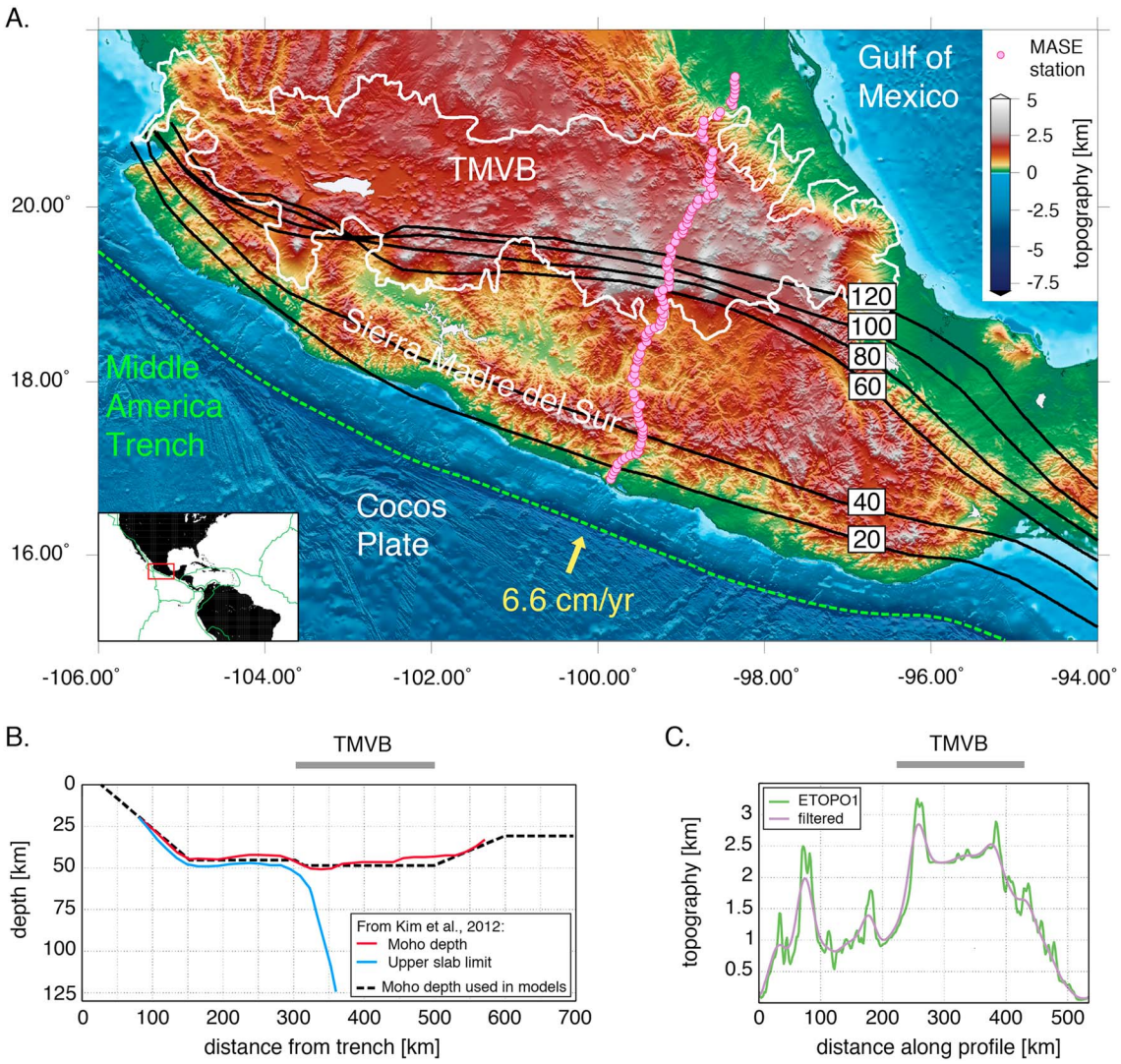

Figure 1. (a) Geodynamic context of southwestern Mexico. Topography and bathymetry from ETOPO1 [*Amante and Eakins*, 2009]. A white curve outlines the Trans-Mexican Volcanic Belt (TMVB) [*Ferrari et al.*, 2012]. The black lines show the isodepths of the Cocos slab at a 20 km interval, using seismicity up to ~45 km depth and tomography below [*Kim et al.*, 2012a]. These slab contours show that distinct topographic domains are associated with variations in slab geometry. The yellow vector shows the relative convergence velocity between the Cocos and North America Plate near Acapulco, holding North America fixed [*DeMets et al.*, 2010]. The pink circles show the locations of the Meso-America Subduction Experiment (MASE) stations. (b) Moho depth (red) and upper slab limit (blue) from *Kim et al.* [2012a, 2013]. The dashed line shows the simplified Moho depth that we used in the numerical models. (c) Measured and smoothed topography along the MASE profile as a function of the distance from the southernmost seismic station, near Acapulco. The topography is smoothed using three passages of a rectangular sliding average of width 15 km.

Billen and Gurnis, 2001; *Funiciello et al.*, 2008; *Capitanio et al.*, 2010; *Stegman et al.*, 2010; *Alisic et al.*, 2012; *Gérault et al.*, 2012; *Holt et al.*, 2015]. In addition, because global computations that account for sharp LVVs remain numerically intensive [*Stadler et al.*, 2010], we opt for 2-D geodynamic models that can incorporate a detailed treatment of the structure of local plate boundaries.

Convergence between the Cocos and North America plates in southwestern Mexico is accommodated by oblique subduction along the Middle America Trench at 6.6 cm/yr near Acapulco [*DeMets et al.*, 2010]. The Trans-Mexican Volcanic Belt (TMVB), a volcanic arc stretching from the Gulf of California to the Gulf of Mexico, is located several hundreds of kilometers inland from the Cocos trench (Figure 1). This intracontinental arc has been active since the mid-Miocene, following the onset of flat-slab subduction [e.g., *Ferrari et al.*, 1999; *Gómez-Tuena et al.*, 2007]. The coastal range of the Sierra Madre del Sur corresponds to the ancient arc that has been inactive since the late Oligocene [*Morán-Zenteno et al.*, 1996; *Ducea et al.*, 2004].

In this study, we focus on a transect from Acapulco to Tempoal, through Mexico City and the central TMVB (Figure 1), where the flat slab is not directly caused by the subduction of thickened oceanic crust [*Skinner and Clayton*, 2011; *Gutscher et al.*, 2000] or by interactions with a proximal lithospheric root as suggested for South America [*O'Driscoll et al.*, 2009, 2012]. Structure beneath this transect was imaged down to ~150 km with the Meso-America Subduction Experiment (MASE), a 100-station, ~500 km long broadband seismic network deployed from 2005 to 2007 [e.g., *Pérez-Campos et al.*, 2008; *Husker and Davis*, 2009; *Chen and Clayton*, 2009; *Kim et al.*, 2010]. The seismic line ran nearly perpendicular to the trench, covering the fore-arc, the arc (the TMVB), and some of the back-arc. The age of the Cocos slab at the trench is only ~14 Ma in this region [*Müller et al.*, 2008]. *Husker and Davis* [2009] inverted *P* wave travel time residuals which they used to infer the thermal parameters of a model and proposed that the slab appears to be ~40 km thick, consistent with a half-space cooling model [e.g., *Turcotte and Schubert*, 2002]. Results from the MASE show that the slab subducts at a ~15° dip angle for the first ~150 km inboard from the trench. Then, at a depth of ~45 km, it turns flat for another ~150 km and eventually bends toward the deep mantle with a 75° dip angle [*Pérez-Campos et al.*, 2008; *Husker and Davis*, 2009; *Iglesias et al.*, 2010; *Kim et al.*, 2010, 2012a]. *P* wave travel time tomography [*Husker and Davis*, 2009] indicates that the slab is not anchored in the lower mantle, reaching at most ~550 km depth. The Cocos slab appears to be truncated in the upper mantle beneath most of southwestern Mexico [e.g., *Ferrari et al.*, 2012]. It has been proposed that the slab detached following the termination of subduction beneath Baja California, resulting in a pulse of mafic volcanism that propagated from west to east [*Ferrari*, 2004; *Orozco-Esquivel et al.*, 2007; *Ferrari et al.*, 2012]. Along the MASE profile, the slab reaches a depth that is consistent with the age of the proposed break-off (~7.5 Ma) and the plate convergence velocities since that time [*Ferrari et al.*, 2012].

The receiver function studies of *Pérez-Campos et al.* [2008] and *Kim et al.* [2010] indicate that the mantle lithosphere is replaced by the Cocos slab in the fore-arc. The hingeline of the flat slab rolled back from the northern edge of the TMVB to its current position [*Ferrari et al.*, 2012], which suggests that the mantle lithosphere should also be missing from beneath the arc and adjacent back-arc. Crustal structure estimates [*Molina-Garza and Urrutia-Fucugauchi*, 1993; *Urrutia-Fucugauchi and Flores-Ruiz*, 1996; *Kim et al.*, 2010, 2012a] indicate that the depth of the continental Moho is nearly uniform beneath the fore-arc (~45 km) and the arc (~45–50 km). Yet their mean elevations differ by more than 1 km (Figure 1c). Interestingly, variations in topography correspond to variations in slab morphology: the Sierra Madre del Sur is located at the transition between shallow and flat subduction; the ~1 km high fore-arc corresponds to the region above the flat slab; and the TMVB (elevations higher than 2 km) begins where the slab plunges toward the deep mantle.

Seismic activity occurs to depth of ~45 km and does not continue north beyond the flat-slab segment [*Suárez et al.*, 1990; *Singh and Pardo*, 1993]. There is no Wadati-Benioff zone where the slab steepens beneath the TMVB. Slow slip events have been reported beneath the Sierra Madre del Sur [e.g., *Brudzinski et al.*, 2007; *Kostoglodov et al.*, 2010; *Radiguet et al.*, 2012; *Song and Kim*, 2012], and bursts of nonvolcanic tremor [e.g., *Payero et al.*, 2008; *Kostoglodov et al.*, 2010] are frequent above the flat slab, which may indicate a relatively low coupling along the subduction interface. Although flat slabs in South America are associated with increased seismic activity [*Gutscher et al.*, 2000], the MASE profile is adjacent to the "Guerrero seismic gap," a ~2000 km^2 area where no major thrust earthquakes ($M \geq 6.5$) have been recorded since 1911 [*Singh et al.*, 1981; *Nishenko and Singh*, 1987; *Anderson et al.*, 1989]. *Singh and Pardo* [1993] studied small earthquakes in the fore-arc, finding that events near the trench are dominated by thrust mechanisms. In contrast, small earthquakes located in the crust above the flat slab tend to have normal faulting mechanisms, although evidence for extensional tectonics at the surface has not been reported. Overall, the fore-arc appears to be in a nearly neutral state of stress. The TMVB, however, is experiencing a pervasive extension north of the active volcanoes [*Suter et al.*, 2001]. This tectonic stress state differs from other flat slabs, mainly located in South America, where compressive tectonics occurs above the slab hingeline [e.g., *Gutscher et al.*, 2000; *Espurt et al.*, 2008]. Gravitational collapse may only partially explain the tectonic regime in the TMVB [*Suter et al.*, 2001] because extension is more pronounced to the west, closer to the Gulf of California, where the crust is on average ~10 km thinner [*Ferrari et al.*, 2012], than to the east, where the MASE profile is located.

While large-scale stresses are likely influenced by the dynamics of the North America plate, which are controlled by gravitational potential energy variations and basal tractions from mantle flow [e.g., *Humphreys and Coblentz*, 2007; *Ghosh et al.*, 2013], stress patterns in the TMVB appear to be more strongly controlled by variations in the slab geometry: normal faulting began in the northern, older part of the arc and spread toward the south as the slab began to roll back (see *Ferrari et al.* [2012] for a review), suggesting that subduction

processes have a stronger local effect than the action of far-field plate stresses. A north-to-south migration, similar to normal faulting, is observed in the age of volcanism [e.g., *Gómez-Tuena et al.*, 2007; *Cadoux et al.*, 2011; *Ferrari et al.*, 2012].

Singh and Pardo [1993] proposed that normal faulting in the TMVB might be enhanced by trench rollback, and several studies have argued in favor of hot material beneath the arc [e.g., *Fix*, 1975; *Molina-Garza and Urrutia-Fucugauchi*, 1993; *Márquez et al.*, 1999], perhaps caused by slab-driven corner flow [e.g., *Ferrari et al.*, 2012; *Manea et al.*, 2013]. The high-Mg basaltic andesites observed in the TMVB require a high volatile content and temperatures in the range of 1180–1250°C beneath the TMVB [*Weber et al.*, 2012], hinting at relatively low densities and viscosities. In addition, seismic imaging studies [*Pérez-Campos et al.*, 2008; *Iglesias et al.*, 2010; *Kim et al.*, 2012a] indicate a reduction in shear wave speed in the mantle beneath the TMVB, and high *P* [*Chen and Clayton*, 2009], *P*, and *S* wave attenuation [*Chen and Clayton*, 2012]. Detailed converted-wave imaging [e.g., *Kim et al.*, 2010, 2012a] shows that the shallow mantle beneath the TMVB region corresponds to the mantle wedge (i.e., the corner of asthenosphere between the steep slab segment and the continental Moho). Similar mantle wedge properties have been inferred in other subduction zones, although usually below ~100 km depth [e.g., *Barazangi and Isacks*, 1971; *Wiens et al.*, 2008].

Iglesias et al. [2010] used a reduction in shear wave velocities in the mantle wedge and the crust above to infer density variations along the MASE profile. They were able to fit the high TMVB elevations using a Pratt model and a reasonable ratio of density to shear velocity variations. Hence, they proposed that the TMVB is supported isostatically. They could not, however, match the topography in both the arc and the fore-arc with a single conversion factor. In addition to uncertainties in linking shear velocity to density variations, *Iglesias et al.* [2010] assumed that the fore-arc's elevation is isostatic and used it as reference. We show below (see section 2) that this assumption is likely to be incorrect and that the difference in elevation between the TMVB and the fore-arc is primarily a consequence of dynamic, as opposed to isostatic, forces.

In summary, the Mexican flat slab differs from other present-day occurrences because (1) it is associated with abundant arc volcanism, (2) it is associated with extension in the arc and a neutral state of stress in the fore-arc, (3) it generates relatively low seismic activity, (4) the continental mantle lithosphere is very thin or nonexistent, (5) it is not directly caused by the subduction of thickened oceanic crust, and (6) there is no nearby cratonic keel. In this study, we address the contribution of the subducting slab and resulting mantle flow to the topography and stress-strain distribution. We first estimate the component of isostatic topography analytically and then evaluate the relative contribution of the buoyancy from the slab versus the mantle wedge to the topography with numerical modeling. The mechanical properties of the mantle wedge regulate how forces are transmitted between the sinking slab and the upper plate [*Billen and Gurnis*, 2001, 2003; *Čadek and Fleitout*, 2003; *Krien and Fleitout*, 2008], thus exerting first-order control on the topography and stress patterns in overriding plate. Although previous geophysical studies indicate that the nature of the mantle wedge should contribute to the arc elevation, the quasi-uniform Moho depths suggests that subduction dynamics may affect the fore-arc topography to a greater extent. We also evaluate the role of lateral viscosity variations and slab-lower mantle interactions in the topography and stress-strain patterns. The case of southwestern Mexico allows us to better understand the mechanisms that drive continental dynamic topography above flat subduction zones, and its unusual setting allows a unique perspective on this.

2. Isostatic Topography

Our estimates of crustal thicknesses rely on gravimetric [*Molina-Garza and Urrutia-Fucugauchi*, 1993; *Urrutia-Fucugauchi and Flores-Ruiz*, 1996] and seismic imaging studies [*Kim et al.*, 2010, 2012a], which also constrain the mean crustal density as ~2900 kg/m^3 from the fore-arc to the back-arc. In the back-arc, at the northernmost MASE station and farther to the north, the crust is ~30 km thick (Figure 1b) and the elevation is ~150 m (Figure 1). In the TMVB, crustal thickness varies between ~45 and ~50 km, and elevation varies between the ~2300 m high central plateau and the volcanic edifices that sometimes reach over 3000 m. In the fore-arc, the crust averages ~45 km thick and topography averages near 1000 m, with short-wavelength variations of a few hundred meters. Crustal thickness in the Sierra Madre del Sur, where mean elevations are 1500–2000 m, has remained steady since the end of the Oligocene [*Ducea et al.*, 2004].

We compute the isostatic component of the topography following a standard approach [e.g., *Crough and Thompson*, 1976; *Bird*, 1979; *Lachenbruch and Morgan*, 1990]. The slab (flat and inclined segments) is never included in our isostasy calculations. Following *Becker et al.* [2014], we compute the density of the

asthenosphere so as to minimize the role of dynamic effects in the mean elevation, using an average regional crustal thickness and ridge depth. We use the mean depth of the East Pacific Rise in the region of −2800 m, an oceanic crustal thickness of 7 km, the average continental elevation of 1000 m, the assumed crustal density of 2900 kg/m^3, and an average continental crustal thickness of 38 km along the MASE profile (which we extended to the Gulf of Mexico). With these values, assuming that the lithosphere has been removed from across our study area (see section 1) and therefore taking the base of the crust as the compensation depth, we calculate an asthenosphere density of ∼3200 kg/m^3. The effect of assuming a greater asthenospheric density is discussed below.

Assuming Airy isostasy, we compute the expected elevation difference between the fore-arc, the arc, and the back-arc, using representative crustal thicknesses of 45, 48, and 30 km, respectively, based on the previously mentioned seismic imaging studies (Figure 1b). Accordingly, the elevation difference between a 30 km and a 48 km thick crustal block is 1860 m. The mean back-arc elevation of ∼150 m thus indicates that the expected isostatic elevation of the TMVB is ∼2000 m. This is ∼400 m lower than the typical elevation in the central plateau. Using a mean crustal density of 2850 kg/m^3 instead would result in an isostatic elevation difference of 2210 m, close to the actual value, while using a density of 2950 kg/m^3 would yield 1530 m. Using a greater asthenospheric density of 3250 kg/m^3 instead would predict an isostatic elevation of ∼2300 m for the TMVB, about the actual value. These calculations suggest that the current elevation of the TMVB could be purely or nearly isostatic. Following the same numerical approach, we compute a deficit in elevation of the fore-arc relative to the arc of 310 m (and 370 m using a crustal density of 2850 kg/m^3 and 250 m using 2950 kg/m^3). These results indicate that forces below the fore-arc crust should be responsible for an additional ∼1 km drop in elevation between the fore-arc and the arc.

In order to constrain the effect of the Cocos slab on topography, we compute the difference in isostatic elevation expected between a column of fore-arc and a column of arc, taken from the surface to the base of the flat slab. In the fore-arc, we use a 45 km thick continental crust, on top of a 4 km thick weak zone of density 3200 kg/m^3 (similar to that of the asthenosphere), and a 7 km thick oceanic crust of density 2900 kg/m^3. We neglect thermal contraction and assign the density anomaly of the subducting mantle lithosphere to a uniform 60 kg/m^3. Hence, the lowest layer corresponds to a 40 km thick slab [*Husker and Davis*, 2009] of density 3260 kg/m^3. These 4 layers form a 96 km thick fore-arc column. Accordingly, the arc column is composed of 48 km of asthenosphere in addition to 48 km of continental crust. These densities and layer thicknesses are also used in the numerical models in section 3.2. This calculation predicts an elevation difference of 375 m between the arc and the fore-arc when accounting for the weight of the slab. Using a greater asthenosphere density of 3250 kg/m^3 predicts an elevation difference of 307 m instead. Using a slab density anomaly of, for instance, 80 kg/m^3 would predict a difference of 625 m, whereas an anomaly of 40 kg/m^3 would predict a difference of 125 m. These estimates range between one tenth and one half of the actual elevation drop between the arc and the fore-arc. However, they do not include the dynamic effects of subduction-driven mantle flow. We explore this contribution in the following section.

3. Models of Mantle Flow

3.1. Methods

We use a 2-D cylindrical finite element code adapted from MILAMIN [*Dabrowski et al.*, 2008; *Gérault et al.*, 2012] that solves for the velocity and pressure fields using a Stokes flow formulation with a Newtonian rheology. The models are instantaneous, and the density and viscosity fields are assigned and uniform throughout structural domains (Figure 2 and Table 1). We ran time-evolving models where we simply advected the nodes proportionally to the velocity field. At no point was there a sign of imbalance, such as a significant change in the velocity field, so we are confident that this geometry, in spite of being imposed, does not cause artifacts. The upper and lower boundary conditions are free slip. The cylinder is truncated on each side, where the boundaries are also free slip. Figure 2 shows the different phases and parameters used in the model, as well as the full size of the computational domain.

The morphology of the two plates that represent the Cocos and North America plates is based on seismic images from the MASE profile (see section 1). They are implemented using an unstructured triangular mesh that allows for an accurate discretization of complex geometries. The numerical resolution (distance between nodes) is ≤500 m at the surface and along all phase boundaries (plates, slab, wedge, and weak zones) and

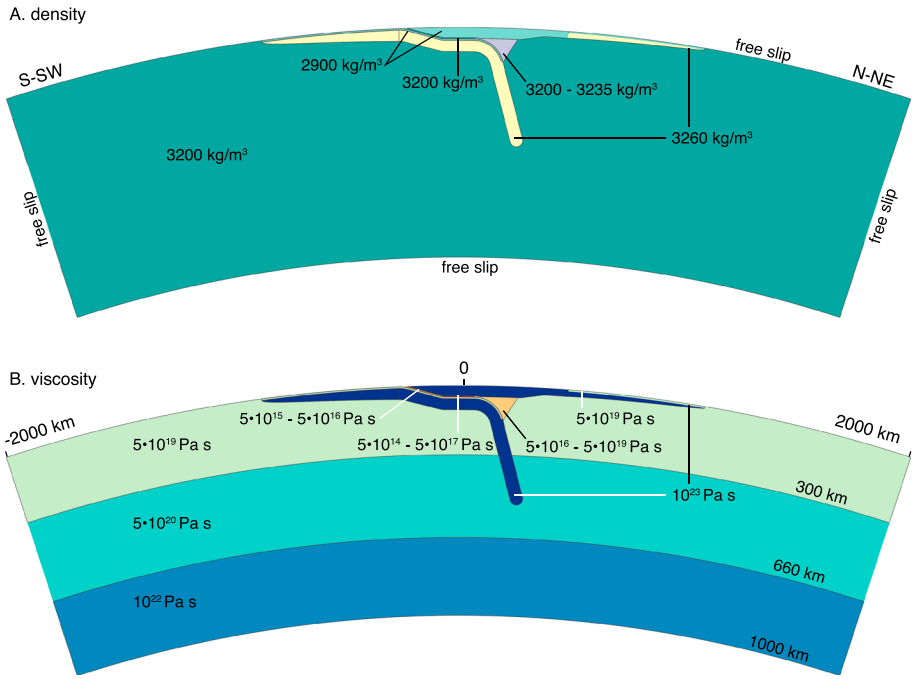

Figure 2. Structure in (a) density and (b) viscosity with boundary conditions. See also Table 1.

up to 20 km in the lower mantle. Oceanic plate thickness follows a half-space cooling model [e.g., *Turcotte and Schubert*, 2002] so as to account for the gravitational effect of the ridge, i.e., ridge push. The slab is 40 km thick and extends to a maximum depth of 500 km [*Husker and Davis*, 2009], aside from one model (model C) where it is anchored in the lower mantle, extending to a depth of 700 km. Compared to the seismic profile, a short segment of oceanic lithosphere is added to the northern side of the overriding continental plate, as to mimic the passive margin with the Gulf of Mexico. Our knowledge of the wedge geometry suggests that it begins below the continental Moho [*Chen and Clayton*, 2009, 2012; *Kim et al.*, 2012a; *Iglesias et al.*, 2010] and reaches at least 120 km depth [*Chen and Clayton*, 2009]. For simplicity, we use the same wedge geometry in all models. Vertically, it is defined between the base of the overriding plate (45 to 48 km) and a maximum depth of 150 km; horizontally, it extends 200 km beyond the tip of the flat-slab segment, below the TMVB. On the basis of the observations described in section 1, we use a uniform crustal thickness of 45 km above the flat slab (beneath the fore-arc) and 48 km beneath the arc. Farther north, the crust tapers off linearly to 30 km. The simplified Moho geometry that we use, as well as the original data, are shown in Figure 1b. We use a uniform crustal density of 2900 kg/m^3 for the continental crust [e.g., *Molina-Garza and Urrutia-Fucugauchi*, 1993; *Kim et al.*, 2012a]. The fault zone between the subducting oceanic crust and the overriding plate is modeled with a 4 km wide weak zone. The role of that interface depends on both the width and the viscosity of the weak zone. We eliminate this trade-off by holding the width fixed and as narrow as numerically convenient and test the effect of the viscosity in the weak zone and in wedge over several orders of magnitude. The slab viscosity is 500 times stiffer than the upper mantle [e.g., *Funiciello et al.*, 2008]. The values of most physical and geometrical parameters are summarized in Table 1.

3.2. Numerical Results

In our modeling, we hold the density and thickness of the crust and slab fixed. Then, the primary controls on topography and overall stress state in the upper plate are the viscosities of the subduction interface and the mantle wedge, and the extent of slab anchoring into the lower mantle. The predicted topography is computed along the upper boundary using the vertical stress there. The isostatic topography, calculated from the model crustal density and thickness, is subtracted from the model-predicted topography to obtain our estimate of dynamic topography.

We present a series of models with different subduction properties, as shown in Table 2. Model A presents the case in which the mantle wedge viscosity is the same as the rest of the asthenosphere, and the viscosity is moderate along the shallow and flat subduction interface (Figure 3). Model B differs by the addition of a weak

Table 1. Physical and Geometrical Parameters in Numerical Modeling of Mexico[a]

Parameters	Values
Density (kg/m^3)	
Continental and oceanic crust	2900
Weak zones (subduction interface)	3200
Asthenosphere, upper and lower mantle	3200
Oceanic lithosphere	3260
Viscosity (Pa s)	
Upper mantle (reference)	$5 \cdot 10^{20}$
Oceanic lithosphere and continental crust	10^{23}
Oceanic crust	$5 \cdot 10^{19}$
Weak zones (subduction interface)	$5 \cdot 10^{14}$ to $5 \cdot 10^{17}$
Asthenosphere	$5 \cdot 10^{19}$
Mantle wedge (above the slab)	$5 \cdot 10^{16}$ to $5 \cdot 10^{19}$
Lower mantle	10^{22}
Geometry (km)	
Weak zone thickness	4
Oceanic crust thickness	7
Continental crust thickness	30 to 48
Asthenosphere to upper mantle transition depth	300
Upper to lower mantle transition depth	660
Maximum slab depth extent	500 to 700
Slab thickness	40
Flat slab segment length	150
Depth of mantle wedge area	45 to 150
Overriding plate length	700
Cocos plate length	600

[a]See also Figure 2.

mantle wedge, where the viscosity is intermediate between that in the weak zones and that in the asthenosphere. Model C highlights how a slab anchoring into in the lower mantle, which is unlike that observed in southwestern Mexico, would affect the results. To better understand how the coupling along the flat slab controls the predictions of topography and stress in the overriding plate, we then show two end-member models where the viscosity is increased (model D) or reduced (model E) by up to 2 orders of magnitude with respect to model B. The role of lateral viscosity variations is then examined in the isoviscous equivalent of model B. Lastly, we present our preferred model (model F), which is similar to model B but with a density reduction in the wedge. For each model, we show the topography and its isostatic and dynamic components, and the deviatoric stress and velocity fields. In addition, the dynamic pressure and strain rates are shown in the supporting information.

3.2.1. Role of the Viscosity in the Mantle Wedge

Model A represents a simple case where the asthenospheric viscosity is uniform, as opposed to reduced locally in the mantle wedge. Suction in the slab corner causes up to ~1.3 km of negative dynamic topography (Figure 3a, green curve). This behavior was previously described by *Billen and Gurnis* [2001, 2003]. Model A cannot reproduce the step-like transition in the topography between the fore-arc and the TMVB. Some amount of decoupling in the mantle wedge is required for the TMVB to form a broad plateau that stands close to its isostatic elevation. While extension is predicted throughout the overriding plate, the deviatoric stress is significantly larger in the TMVB, suggesting a greater propensity for faulting throughout the arc than in the fore-arc and the back-arc (Figure 3b). This indicates, unlike previously suggested (see section 1), that extension in the TMVB can be predicted in a model without a viscosity reduction in the mantle wedge. The location of the viscosity transition between the horizontal weak zone and the wedge has a small influence on the predicted topography pattern but does not modify where the apex of the downwarping is located. Below 300 km depth, the velocity vectors are steeper than the slab dip, indicating a tendency for the deeper part of the slab

Table 2. Main Variables and Corresponding Models[a]

	Maximum Slab Depth (km)	Δ_w	η_t	η_f	η_w
Model A	500	0	10^{-4}	10^{-5}	10^{-1}
Model B	500	0	10^{-4}	10^{-5}	10^{-3}
Model C	700	0	10^{-4}	10^{-5}	10^{-3}
Model D	500	0	10^{-4}	10^{-3}	10^{-3}
Model E	500	0	10^{-5}	10^{-6}	10^{-4}
Model F	500	35	10^{-4}	10^{-5}	10^{-3}

[a]Maximum depth extent of the slab (anchored in the lower mantle if $\leq$ 660 km); Δ_w: density contrast between the wedge and the asthenosphere (in kg/m^3, positive for a positively buoyant wedge); η_t: ratio of the weak zone viscosity at the trench to the viscosity of the upper mantle; η_f: viscosity ratio of the weak zone above the flat slab to the upper mantle; η_w: viscosity ratio of the wedge to the upper mantle.

to roll back. At shallower depths, it is the downgoing motion of the slab that draws mantle flow into the slab corner, resulting in a gradient in the mantle velocity at the base of the upper plate. The greatest strain rates (see Figure S1b in the supporting information) occur along the subduction interface and in the mantle wedge, where the viscosity is the lowest.

The models shown in Figures 4 and 5 incorporate the influence of a viscosity drop in the mantle wedge. Model B is the same model as model A, except for a mantle wedge viscosity reduction by 2 orders of magnitude with respect to the asthenosphere. The buoyancy of the wedge remains neutral (identical to that of the surrounding mantle). This could represent a hypothetical case where the wedge is weakened by fluids from the slab, but where the temperature remains unchanged with respect to the rest of the asthenosphere. Model B predicts an abrupt increase in elevation going from the arc to the fore-arc (Figure 4a). The low-viscosity wedge allows the TMVB to stand near its isostatic elevation (minor dynamic influence), while the mass anomaly from the flat slab causes the fore-arc to subside by ~700 m. Figure 4a shows that the dynamic topography created by the flat slab exceeds that induced by an equivalent static density anomaly (cf. section 2) and can account to a large extent for the elevation difference between the arc and the fore-arc, the rest likely owing to variations in crustal thickness and mantle wedge buoyancy. The light blue and purple curves in Figure 5 show the dynamic topography of models A and B, as well as the effect of other mantle wedge viscosities from models not shown. Figure 5 shows that the elevation of the arc and the adjacent fore-arc is strongly controlled by the

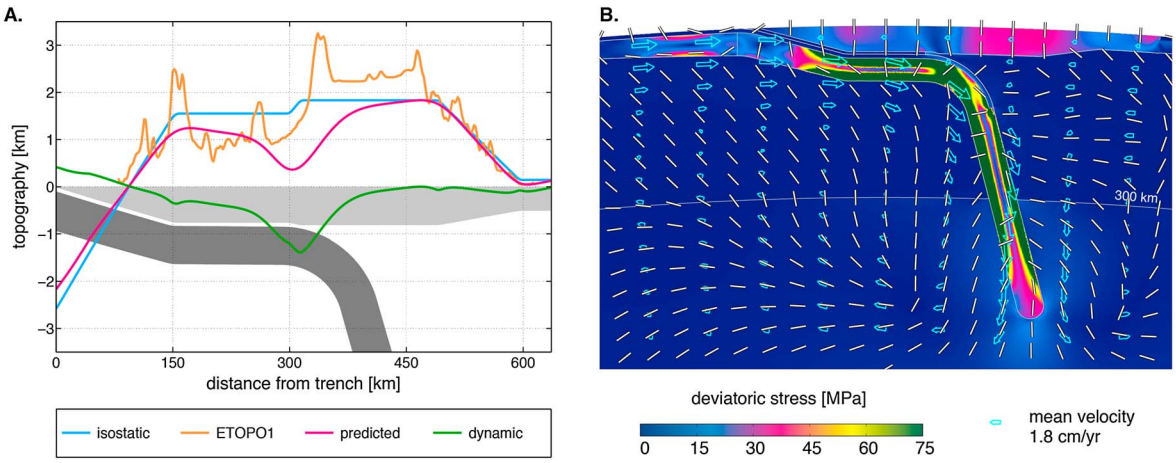

Figure 3. No distinction between the mantle wedge and the asthenosphere (model A). (a) Topography as a function of the distance from the trench. The pink curve shows the topography predicted by the model. The isostatic elevation (blue curve) is computed with Airy isostasy between the surface and the deepest level of the crust (48 km). The dynamic topography (green curve) is the model prediction subtracted from the isostatic elevation. MASE elevation data (orange curve) from ETOPO1 (as in Figure 1c). The outline of the slab, the wedge, and the upper plate are shown in the background in shades of dark, light, and medium grey, respectively. (b) Second invariant of the deviatoric stress tensor (colored background), most compressive, principal stress axis (white sticks), and velocity field (arrows). The dashed line indicates the mantle wedge region.

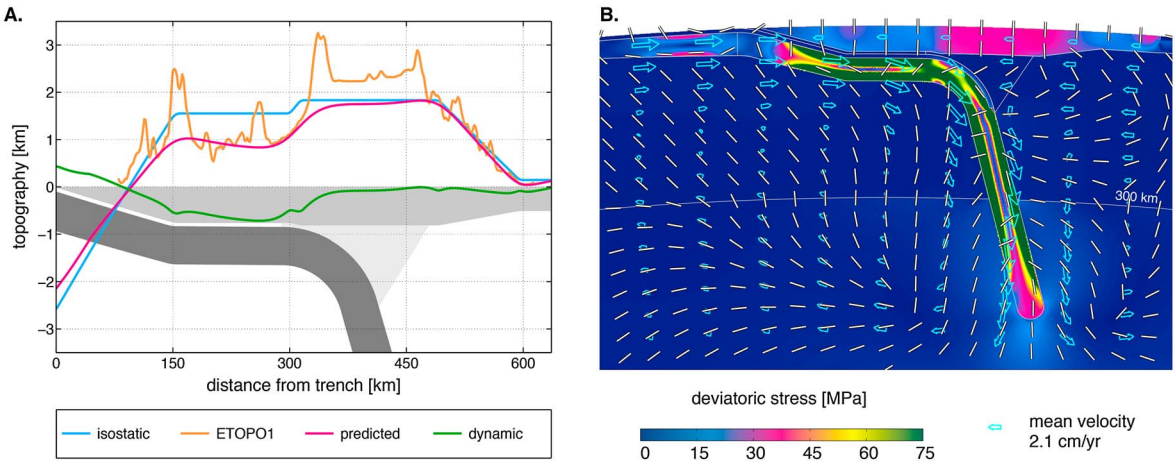

Figure 4. Role of a viscosity decrease in the mantle wedge (model B). See Figure 3 for detailed caption.

wedge viscosity. While a significant viscosity reduction is required for the arc not to subside, models with a very low wedge viscosity fail to predict hundreds of meters of elevation difference between the arc and the fore-arc as observed in southwestern Mexico. In addition to its influence on topography, the addition of a weak mantle wedge has a modest effect on plate velocities: subduction velocity increases from ~4.5 to ~5 cm/yr. The modeled convergence velocity is larger than that of *DeMets et al.* [2010] by less than 1 cm/yr. The addition of a weak wedge enables in a slightly broader region of high extensional stress, but the maximum amplitude and general pattern remain similar to the case without a weak wedge.

3.2.2. Role of Slab Anchoring Into the Lower Mantle

Unlike other flat slabs, such as in South America, the Cocos slab does not extend down to the lower mantle. In model C, we look at the predictions of a model similar to model B, except that the slab extends into the lower mantle to a depth of 700 km. This has a large impact on the topography and the mantle flow velocities. The Stokes velocity depends directly upon the viscosity of the surrounding medium and the square of the size of the sinking body [e.g., *Batchelor*, 1967]. Increasing the length of the slab tends to increase the sinking velocity, while greater viscous resistance in the lower mantle tends to lower the velocity. In model C, the average mantle flow velocities decrease by a factor of ~5. Slab anchoring in the lower mantle results in virtually no subsidence in the overriding plate (Figures 6a and 7), very slow flow velocities (0.4 cm/yr on average; Figure 6b), and pervasive extension. This extension is driven by a high gravitational potential energy (the continental crust) that is unbalanced by the basal tractions applied by the slab. In models A and B, the dynamically unsupported slab creates significant fore-arc subsidence, which is necessarily accompanied by a horizontal compressive

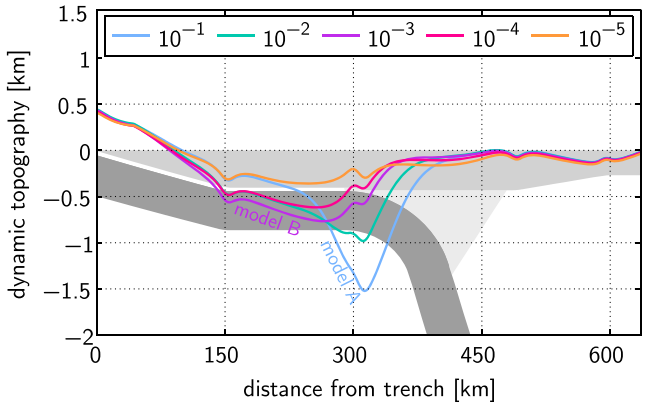

Figure 5. Dynamic topography as a function of the mantle wedge viscosity contrast with respect to the upper mantle. Each curve corresponds to a different viscosity ratio of the wedge to the upper mantle (reference) viscosity. The light blue and purple curves show the dynamic topography in models A and B, respectively. For reference, the outline of the slab, the mantle wedge, and the upper plate are shown in the background in shades of dark, light, and medium grey, respectively.

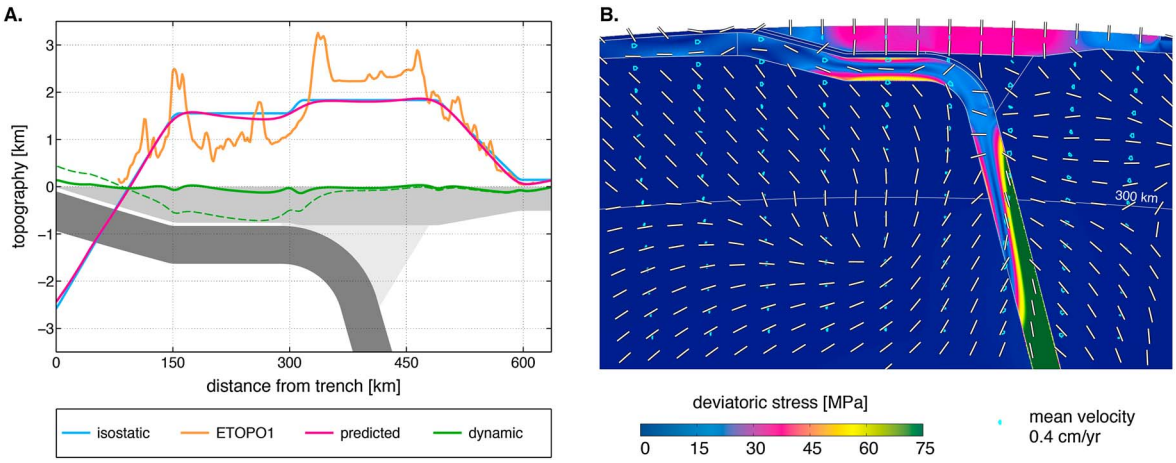

Figure 6. Role of the slab-lower mantle interactions (model C). See Figure 3 for detailed caption. In Figure 6a the dashed green line shows the dynamic topography from model B (Figure 4) for reference.

stress component. Hence, negligible fore-arc extension in models A and B results from the combination of overall upper plate extension with dynamic subsidence localized above the flat slab. In model C, however, the slab is supported by the lower mantle and has very little effect on stress in the upper plate.

Figure 7 shows dynamic topography as a function of the viscosity ratio of the lower mantle to the upper mantle. In these models, the slab is anchored in the lower mantle as in model C and the lower mantle viscosity varies. The case where the radial viscosity structure of the mantle is uniform (green curve in Figure 7) predicts both positive and negative dynamic topography, from ~1 km of uplift near the trench to ~1.4 km of subsidence above the flat slab. The stiffer the lower mantle, the smaller the amplitude of the dynamic topography. The pattern observed in southwestern Mexico between arc and fore-arc elevation can only be predicted by low (≤20) viscosity ratios.

These results suggest that the truncation of the Cocos slab above 660 km depth (1) causes the relatively fast subduction velocity in spite of the slab's young age, (2) facilitates the rollback of the deep slab hinge, (3) results in the increase in elevation from the fore-arc plateau to the TMVB, and (4) gives rise to the nearly neutral state of stress in the fore-arc.

3.2.3. Role of the Viscosity Within the Subduction Interface

The occurrence of extensional tectonics in the broad fore-arc south of the TMVB suggests a weak coupling at the subduction interface above the flat-subducting Cocos slab. To investigate the nature of subduction coupling, we distinguish between two weak zones, one extending from the trench to the beginning of the

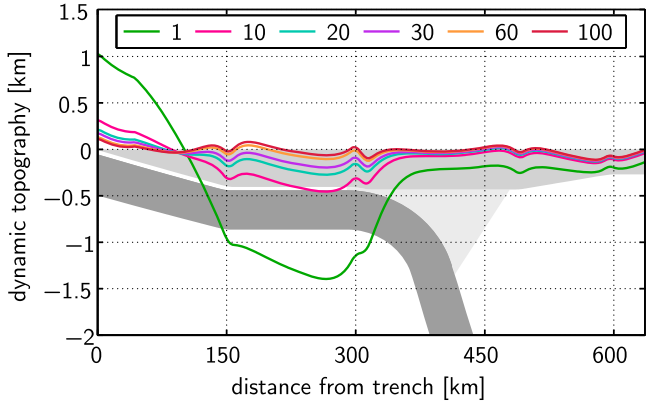

Figure 7. Dynamic topography as a function of the lower mantle viscosity contrast with respect to the upper mantle. Each curve corresponds to a different viscosity ratio of the lower mantle to the upper mantle (reference) viscosity. For reference, the viscosity contrast used in model C is 50. The outline of the slab, the mantle wedge, and the upper plate are shown in the background in shades of dark, light, and medium grey, respectively.

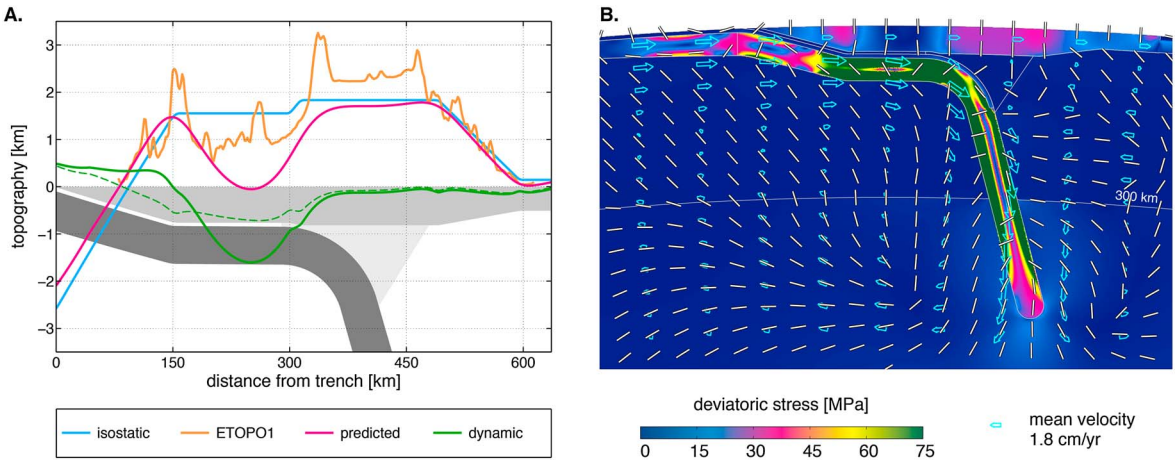

Figure 8. Role of the weak zone viscosity: high coupling (model D). See Figure 3 for detailed caption. In Figure 4a the dashed green line shows the dynamic topography from model B (Figure 4) for reference.

flat segment, and the other above the flat slab. We consider two models that illustrate end-members of high versus low coupling.

Model D (Figure 8) is a case where the viscosity of the horizontal subduction interface, at 4 km thick, is weak but no weaker than in the mantle wedge (i.e., 2 orders of magnitude stiffer than in the models discussed above, see Table 2). The viscosity in both the horizontal weak zone and the wedge is 2 orders of magnitude weaker than the asthenosphere. The viscosity of the subduction interface closest to the trench remains unchanged at a value 10^{-4} orders of magnitude weaker than the asthenosphere, which is required to let subduction occur. Here the topography resembles that above a downwelling centered beneath the flat slab (Figure 8a), which drags the middle of the fore-arc down to sea level (negative dynamic topography $\geq$1.5 km). In the TMVB, the elevation remains relatively close to isostatic and the stress state remains extensional, although lower than in models A and B.

The opposite end-member is a model where the viscosity of the entire subduction interface is particularly weak, as is the wedge (model E, Figure 9). In this case, we use the setup of model B and decrease all weak zones and wedge viscosities by 1 order of magnitude (see Table 2). The subduction interface remains 4 km thick to isolate the role of viscosity. This model shows the opposite effect as the high coupling in model D: it reduces the impact of the slab on the topography. Figure 9a shows that such a viscosity reduction lowers the amplitude of the dynamic topography for both positive and negative values. This is consistent with the idea that the viscosity between the slab and the upper plate controls the transmission of the downward

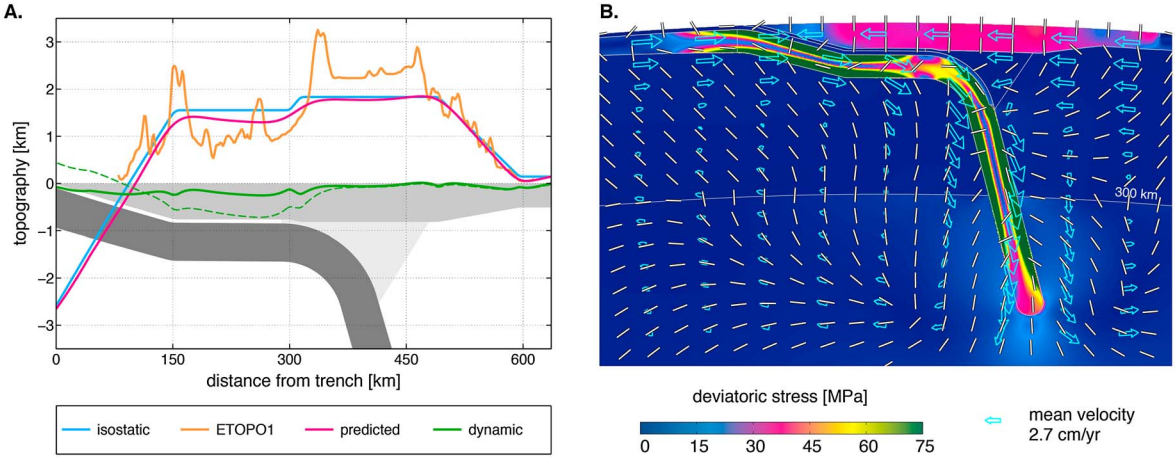

Figure 9. Role of the weak zone viscosity: low coupling (model E). See Figure 3 for detailed caption. In Figure 9a the dashed green line shows the dynamic topography from model B (Figure 4) for reference.

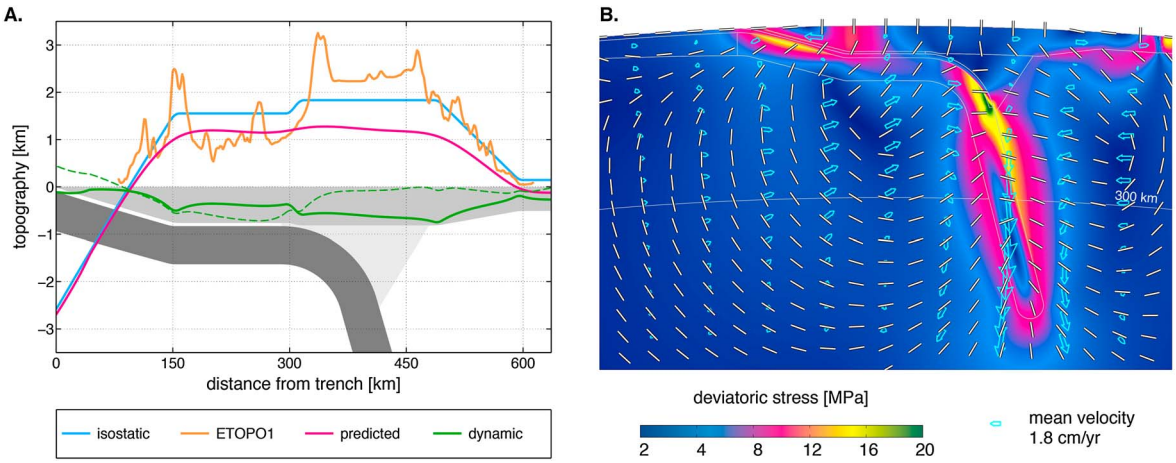

Figure 10. Role of the lateral viscosity variations: isoviscous model with a buoyant upper plate. Density structure as in model B. See Figure 3 for detailed caption. In Figure 10a the dashed green line shows the dynamic topography from model B (Figure 4) for reference.

subduction forces to the surface. It shows that the slab, although it lays flat ~45 km below the surface, would not strongly affect the topography if it were drastically decoupled from the upper plate. In addition, tensile stresses are high throughout the fore-arc and the TMVB. This lends support to the argument that in the fore-arc, the absence of extensional tectonic features and the relatively low elevation are closely related and induced by the interactions between the subducting slab and the overriding plate. Here as in model C, extension is predicted throughout the plate, supporting the idea that extension is not a slab-related feature and that a low-stress fore-arc has to be caused by the flat slab. The reduced viscosities between the slab and the upper plate result in faster subduction velocities (≥ 6 cm/yr) and a convergence velocity that is much greater than at the present day [*DeMets et al.*, 2010].

3.2.4. Role of the Lateral Variations in Viscosity

The results of models A to E differ only in the inclusion of lateral viscosity variations (LVVs). The model shown in Figure 10 is an isoviscous case that employs the same density distribution as in the other models. To help visualize the effect of the slab alone, the same isoviscous model with a neutrally buoyant upper plate is shown in the supporting information in Figure S7. In both isoviscous models, the slab induces a nearly symmetrical mantle flow pattern. This is typical for weak slabs, in which stress guiding is not effective [e.g., *Conrad and Lithgow-Bertelloni*, 2002, 2004; *Gérault et al.*, 2012]. In Figure 10b, the overriding plate extends with divergent velocities on the edges of the plate. In the absence of viscosity variations, the dynamic pressure in the overriding plate is nearly unaffected by the presence of the slab (Figure S6a). Unlike in models A to F, the dynamic topography created by the slab is very broad and always negative (subsidence) or neutral. Without viscosity variations, subsidence is the greatest above the center of mass of the steep segment of the slab, whereas it is otherwise greater above the flat slab because of the enhanced coupling between slab and overriding plate. In isoviscous models, the dynamic topography above the flat slab is similar to that expected from Airy isostasy (i.e., ≤400 m, see section 2), which suggests that in those models the influence of the viscous drag from mantle flow is minor. We conclude that inclusion of viscosity variations better captures the large deficit in fore-arc elevation with respect to the arc. The amplitude of the deviatoric stress shown in Figures 10b and S7b is smaller than in models with LVVs by a factor of ~3, presumably owing to an absence of viscous bending stresses and because resulting stresses are more widely distributed. Deviatoric stress and strain rates (supporting information) are maximum above the steep slab segment. Principal stresses indicate horizontal convergence above 100 km and transition to downdip compression at the tip of the steep slab. Accounting for the low density of the overriding plate has a limited effect on dynamic topography. It does, however, exert a large influence on the distribution of stresses and strain rates in the upper plate.

3.2.5. Preferred Model

Model F (Figure 11 and Table 2) offers the best match to the topography while also matching the tectonic stress state. It is characterized by a moderate viscosity drop along the subduction interface, and a mantle wedge that is weaker and more buoyant than the rest of the asthenosphere. The setup is the same as in model B, but also with a density decrease in the mantle wedge. To obtain ~400 m of positive dynamic topography (cf. section 2), we find that an excess buoyancy of 35 kg/m^3 is required for the wedge geometry that we use. The stress

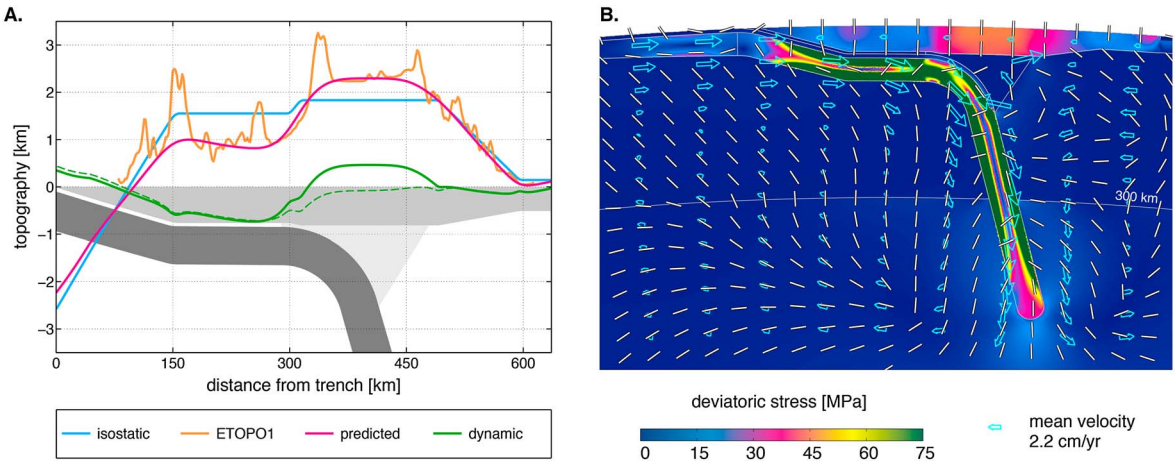

Figure 11. Role of the wedge buoyancy and preferred model (model F). See Figure 3 for detailed caption. In Figure 11a the dashed green line shows the dynamic topography from model B (Figure 4) for reference.

pattern in the overriding plate is similar to model B (Figure 4b), but the buoyant wedge induces additional extension in the TMVB (Figure 11b). The low density of the wedge causes a linear increase in wedge pressure (see Figure S8a in the supporting information) and upward flow. As a result, a small cell of clockwise convection develops within the larger, counterclockwise corner flow pattern. This type of small-scale counterflow in a weak and buoyant wedge was also observed in the models of *Davies and Stevenson* [1992] and *Billen et al.* [2003]. The plate convergence velocity that is nearly equal to that observed [*DeMets et al.*, 2010].

4. Discussion

4.1. The Unusual Characteristics of the Flat Slab in Southwestern Mexico

The Cocos slab is nearly horizontal between Acapulco and Mexico City. Although there are other flat slabs along the western margin of the Americas, such as Alaska, Peru, and Chile-Argentina, the tectonic setting surrounding the slab in southwestern Mexico is unique. The absence of thickened oceanic crust [*Skinner and Clayton*, 2011; *Gutscher et al.*, 2000], lithospheric mantle [*Pérez-Campos et al.*, 2008; *Kim et al.*, 2012a; *Ferrari et al.*, 2012], and nearby continental keel results in an unusual density and viscosity structure. It is therefore an interesting place to study the effects of slab-induced dynamic topography.

Skinner and Clayton [2011] examined the possible reasons for slab flattening and concluded by elimination that it could come from a low-viscosity wedge, as proposed earlier by *Manea and Gurnis* [2007]. We briefly propose an alternative explanation. Although no buoyant seafloor features subducted where the slab is currently flat [*Skinner and Clayton*, 2011], it appears that slab flattening occurred during the Oligocene [*Ferrari et al.*, 2012], a process that would have been promoted by the young age of the Cocos plate and the subduction of buoyant seafloor features. The current flat slab is located in the middle of two presumed tears [*Stubailo et al.*, 2012; *Dougherty and Clayton*, 2014] which may have isolated this portion of slab from those to either side, where the slab subducts with a more typical dip. The ultimate cause of slab flattening, however, is not yet understood.

Abundant volcanism in the TMVB contradicts the usual assumption that flat slabs shut down arc magmatism [e.g., *Isacks and Barazangi*, 1977; *Jordán et al.*, 1983; *Bird and Baumgardner*, 1984]. This, and the apparent weak coupling at the subduction interface [*Song et al.*, 2009; *Kim et al.*, 2010, 2012b, 2013], could result from an increased water input into the mantle with respect to other flat slabs. There may be several reasons for this. The slab flattens at the shallow depth of 45 km, perhaps transporting the hydrated slab to the mantle wedge before much of the water has been released through metamorphic reactions. Also, the fact that the flat slab is not associated with the subduction of thickened oceanic crust implies that it is not related to an anomalous melting event, which would have left the crust and the underlying mantle dry. In addition, *Skinner and Clayton* [2011] note that significant tectonic erosion has taken place since the Oligocene and that the subducted erosion products should transport large amounts of water to the mantle. This compares favorably with our dynamic models that suggest that a low-viscosity subduction interface is required to match the topography.

4.2. The Role of the Mantle Wedge and the Subduction Interface Properties

Our numerical results suggest that low-viscosity regions are required in both the mantle wedge and along the subduction interface to capture the upstepping topography as the TMVB is approached, and the nearly neutral stress across the fore-arc plateau. Too much coupling between the overriding plate and the slab causes the topography in the arc and fore-arc to drop below its actual value; too little coupling and the influence of the slab on the fore-arc topography becomes negligible, leaving the fore-arc at a similar altitude as the TMVB, as dictated by its crustal buoyancy. It is the low viscosity of the wedge that prevents the TMVB from being pulled down by the sinking slab [e.g., *Billen and Gurnis*, 2001], while it is the viscosity of the subduction interface that controls the elevation in the fore-arc. We conclude that a weak channel, as previously imaged seismically, is required between the flat slab and the overriding plate to avoid horizontal compression in the fore-arc, in agreement with the study of *Manea and Gurnis* [2007]. We show in section 2 that a few hundred meters of the TMVB elevation could arise from dynamic support, perhaps owing to the presence of melt in the crust beneath the arc or in the mantle wedge. For simplicity, we focus on the wedge buoyancy and find that a density decrease of 35 kg/m^3 creates a good match to the TMVB elevation (see Figure 11). Such a density reduction is larger than the values found by *Billen and Gurnis* [2003] in the Tonga-Kermadec and Central Aleutian subduction zones (20 and 10 kg/m^3, respectively). However, our study uses a slightly different wedge geometry and involves a different setting. Furthermore, there is a trade-off between the density reduction and the volume of the wedge; the results are only sensitive to the net buoyancy. Unlike *Billen and Gurnis* [2001], we find no difference in the topography predicted by models where the viscosity reduction is localized in the wedge as opposed to throughout the asthenosphere (models with a weaker asthenosphere not shown because their results are essentially the same). However, seismic observations discussed in section 1 and the additional buoyancy required to support the TMVB elevation lend support to the presence of a rheologically distinct region between the steep Cocos slab segment and the continental Moho.

4.3. Model Assumptions and Limitations

Our study is designed to identify the mechanisms that control the elevation distribution and crustal stress at the scale of southwestern Mexico, and the trends that we describe are robust in terms of how the viscosity in the wedge and the weak zones affects the topography and stress in the overriding lithosphere. However, the short-wavelength (flexurally supported) topographic features such as the Sierra Madre del Sur and volcanic edifices in the TMVB are absent from our analysis, and we use uniform crustal density and viscosity values throughout the arc system, including uniform crustal thicknesses in each the arc and the fore-arc. Also, if our assumption that there is no mantle lithosphere beneath the TMVB is incorrect, our calculation of the isostatic TMVB elevation would be correspondingly in error. The density of our modeled slab is independent of age. Series of tests with end-member slab density anomalies show that our results can be reproduced using different absolute viscosities for the weak zones along the subduction interface (higher slab densities require less coupling to produce similar subsidence and vice versa). We modeled the slab using a viscosity increase of 500 with respect to the upper mantle [e.g., *Funiciello et al.*, 2008]. However, the Cocos slab is young and could be less viscous than average. We show in the supporting information (Figure S9) that a model where the slab viscosity is 1 order of magnitude lower than in our preferred case provides a similarly good fit to the topography when using a weak zone viscosity 1 order of magnitude higher above the flat slab (keeping other parameters unchanged). Because of these types of trade-off, and because we use a purely viscous Newtonian rheology, the viscosity values that we used are simply representative of effective viscosity trends. Our model profile, located at the center of the flat slab rather than near the slab edges, has the advantage of minimizing the 3-D effects [e.g., *Piromallo et al.*, 2006]. However, the geometry of the Cocos slab varies along the Middle America Trench, suggesting that a 3-D model could place additional constraints on the mechanisms required to match the topography and tectonics in the arc and fore-arc. Our 2-D geometry allows for a detailed treatment of the subduction zone geometry ($\geq$ 500 m numerical resolution) in purely dynamic models (plate motions are driven by buoyancy anomalies only, as opposed to prescribed). These aspects of our modeling are crucial to the questions that we address.

4.4. General Implications

Modeling studies of dynamic topography at subduction zones rarely include a detailed treatment of the lithosphere density and viscosity variations. As a result, constraining dynamic topography amplitudes has proven difficult [*Dávila and Lithgow-Bertelloni*, 2013; *Flament et al.*, 2013]. In this study, we are able to infer

the magnitude of the dynamic response to flat slab subduction by focusing on a present-day example where the properties of the slab and the upper plate are reasonably well constrained. Topography is primarily controlled by the density field, including that of the sublithospheric mantle, but at a subduction zone it also depends significantly on the viscosity structure including the subduction interface, mantle wedge, and the shallow and deep slab. Many previous studies of dynamic topography at subduction zones and elsewhere have involved Stokeslet types of semi-analytical models (see reviews by *Dávila and Lithgow-Bertelloni* [2013], *Flament et al.* [2013]) in which only radial viscosity variations are used, and these models have been successful at explaining the first-order topography. At wavelengths $\geq$ 500 km, the amount of subsidence predicted by our isoviscous and LVVs models is in broad agreement with these models. Nevertheless, our results highlight the significant role of plate boundary rheology in controlling the surface elevation response to mantle flow. In particular, our models only capture the regional topographic variations in southwestern Mexico when lateral viscosity variations (i.e., the more viscous slab, and the weak subduction interface and mantle wedge) are included. This is in agreement with the recent study of *Kaban et al.* [2014] who found that LVVs at plate boundaries have a significant effect on the geoid, mostly through their impact on dynamic topography. While it is often assumed that dynamic topography mostly plays a role at long wavelengths (i.e., beyond ~300 km [*Dávila and Lithgow-Bertelloni*, 2013]), our results show that there is an important shorter-wavelength correspondence between dynamic topography and subduction geometry in southwestern Mexico. This suggests that mantle dynamics can influence topography at wavelengths as short as a few tenth of kilometers, but that previous geophysical models lacked the spacial resolution to capture this behavior.

5. Conclusions

We propose that a combination of characteristics specific to southwestern Mexico—flat-slab subduction without buoyancy anomaly on the Cocos plate, presence of a weak and perhaps buoyant mantle wedge, lack of slab anchoring into the lower mantle, absence of mantle lithosphere beneath the continental crust, and a weak subduction interface—is responsible for a neutral to extensional state of crustal stress and the abrupt elevation increase going from the fore-arc to the arc. We provide numerical models that capture these aspects when lateral viscosity variations from the wedge, subduction interface, and slab are taken into account. The physical properties of the wedge primarily control the topography in the arc (TMVB), whereas those of the subduction interface control the topography and state of stress in the crust.

We attribute the overall extensional stress in the TMVB to its high gravitational potential energy, which is a result of its thin or absent mantle lithosphere. A density reduction in the wedge, while being a contributing factor, is not required for the models to predict extension. Extension is negligible in the fore-arc, where the continental lithosphere is clearly missing and is replaced by the flat Cocos slab. The gravitational potential energy in this region, while large [*Humphreys and Coblentz*, 2007], is kept from being exceptionally great by the weight of the flat slab, which induces subsidence and hence creates a component of horizontal compression in the overriding plate. This results in a nearly neutral fore-arc stress state.

The mass anomaly from the flat slab causes dynamic subsidence of the fore-arc, which accounts for most of its kilometer-scale elevation deficit with respect to the TMVB. The greater the coupling in the wedge and along the subduction interface (i.e., the higher the viscosity), the greater the dynamic subsidence. The fore-arc stands nearly 1 km below its predicted isostatic elevation, which we explain by (1) the lack of slab anchoring into the lower mantle (the Cocos slab stopping at ~500 km depth), (2) an absence of buoyancy anomaly on this flat-slab segment, and (3) low to moderate coupling along the subduction interface. We estimate that the central plateau of the TMVB stands several hundred meters above its crustally predicted isostatic elevation, which requires a low-viscosity mantle wedge to decouple the upper plate from the downgoing slab, and perhaps some contribution from a low-density mantle wedge.

More generally, our study suggests that accurately modeling the wavelength and the magnitude of dynamic topography in a complex geological setting requires a detailed treatment of both the density and the viscosity field. While the tectonic setting of southwestern Mexico is unusual, these results have implications for both regional and global studies that aim at understanding mantle-lithosphere interactions and their surface response, such as sea-level change and the vertical motions of continents.

Acknowledgments
We thank YoungHee Kim for sharing the Cocos slab contours and the geographic location of the MASE stations, as well as Luca Ferrari for sharing the outline of the Trans-Mexican Volcanic Belt, all shown in Figure 1a, which was made with GMT [*Wessel et al.*, 2013]. We thank the Editor John Geissman, Associate Editor Jeroen van Hunen, and reviewer Gabriele Morra for their insightful comments. This work benefited from discussions with Boris Avdeev and others at the 2011 CIDER Summer program, funded by NSF grant EAR1135452. Thorsten Becker provided feedback on an earlier version of the manuscript. M.G. and L.H. were partially supported by ANR grant GiSeLE. All data for this paper are available by contacting the corresponding author at gerault@usc.edu.

References

Alisic, L., M. Gurnis, G. Stadler, C. Burstedde, and O. Ghattas (2012), Multi-scale dynamics and rheology of mantle flow with plates, *J. Geophys. Res.*, *117*, B10402, doi:10.1029/2012JB009234.

Amante, C., and B. W. Eakins (2009), ETOPO1 1 arc-minute global relief model: Procedures, data sources and analysis, *NOAA Tech. Memorandum NESDIS NGDC-24*, US Department of Commerce, National Oceanic and Atmospheric Administration, National Environmental Satellite, Data, and Information Service, National Geophysical Data Center, Marine Geology and Geophysics Division, Boulder, Colo.

Anderson, J. G., S. K. Singh, J. Espindola, and J. Yamamoto (1989), Seismic strain release in the Mexican subduction thrust, *Phys. Earth Planet. Inter.*, *58*, 307–322.

Barazangi, M., and B. Isacks (1971), Lateral variations of seismic-wave attenuation in the upper mantle above the inclined earthquake zone of the Tonga Island Arc: Deep anomaly in the upper mantle, *J. Geophys. Res.*, *76*, 8493–8516.

Batchelor, G. K. (1967), *An Introduction to Fluid Dynamics*, Cambridge Univ. Press, Cambridge, U. K.

Becker, T. W., C. Faccenna, E. D. Humphreys, A. R. Lowry, and M. S. Miller (2014), Static and dynamic support of western United States topography, *Earth Planet. Sci. Lett.*, *402*, 234–246, doi:10.1016/j.epsl.2013.10.012.

Billen, M. I., and M. Gurnis (2001), A low viscosity wedge in subduction zones, *Earth Planet. Sci. Lett.*, *193*, 227–236.

Billen, M. I., and M. Gurnis (2003), Comparison of dynamic flow models for the Central Aleutian and Tonga-Kermadec subduction zones, *Geochem. Geophys. Geosyst.*, *4*, 1035, doi:10.1029/2001GC000295.

Billen, M. I., M. Gurnis, and M. Simons (2003), Multiscale dynamics of the Tonga-Kermadec subduction zone, *Geophys. J. Int.*, *153*, 359–388.

Bird, P. (1979), Continental delamination and the Colorado Plateau, *J. Geophys. Res.*, *84*, 7561–7571.

Bird, P., and J. Baumgardner (1984), Fault friction, regional stress, and crust-mantle coupling in Southern California from finite element models, *J. Geophys. Res.*, *89*, 1932–1944.

Brudzinski, M., E. Cabral-Cano, F. Correa-Mora, C. DeMets, and B. Márquez-Azúa (2007), Slow slip transients along the Oaxaca subduction segment from 1993 to 2007, *Geophys. J. Int.*, *171*, 523–538.

Čadek, O., and L. Fleitout (2003), Effect of lateral viscosity variations in the top 300 km of the mantle on the geoid and dynamic topography, *Geophys. J. Int.*, *152*, 566–580.

Cadoux, A., Y. Missenard, R. G. Martinez-Serrano, and H. Guillou (2011), Trenchward Plio-Quaternary volcanism migration in the Trans-Mexican Volcanic Belt: The case of the Sierra Nevada range, *Geol. Mag.*, *148*, 492–506.

Capitanio, F. A., D. R. Stegman, L. Moresi, and W. Sharples (2010), Upper plate controls on deep subduction, trench migrations and deformations at convergent margins, *Tectonophysics*, *483*, 80–92.

Chen, T., and R. W. Clayton (2009), Seismic attenuation structure in central Mexico: Image of a focused high-attenuation zone in the mantle wedge, *J. Geophys. Res.*, *114*, B07304, doi:10.1029/2008JB005964.

Chen, T., and R. W. Clayton (2012), Structure of central and southern Mexico from velocity and attenuation tomography, *J. Geophys. Res.*, *117*, B09302, doi:10.1029/2012JB009233.

Conrad, C. P., and L. Husson (2009), Influence of dynamic topography on sea level and its rate of change, *Lithosphere*, *1*, 110–120.

Conrad, C. P., and C. Lithgow-Bertelloni (2002), How mantle slabs drive plate tectonics, *Science*, *298*, 207–209.

Conrad, C. P., and C. Lithgow-Bertelloni (2004), The temporal evolution of plate driving forces: Importance of "slab suction" versus "slab pull" during the Cenozoic, *J. Geophys. Res.*, *109*, B10407, doi:10.1029/2004JB002991.

Crough, S. T., and G. A. Thompson (1976), Thermal model of continental lithosphere, *J. Geophys. Res.*, *81*, 4857–4862.

Dabrowski, M., M. Krotkiewski, and D. W. Schmid (2008), MILAMIN: MATLAB-based finite element method solver for large problems, *Geochem. Geophys. Geosyst.*, *9*, Q04030, doi:10.1029/2007GC001719.

Davies, J. H., and D. J. Stevenson (1992), Physical model of source region of subduction zone volcanics, *J. Geophys. Res.*, *97*, 2037–2070.

Dávila, F. M., and C. Lithgow-Bertelloni (2013), Dynamic topography in South America, *J. South Am. Earth Sci.*, *43*, 127–144.

Dávila, F. M., C. Lithgow-Bertelloni, and M. Giménez (2010), Tectonic and dynamic controls on the topography and subsidence of the Argentine Pampas: The role of the flat slab, *Earth Planet. Sci. Lett.*, *295*(1), 187–194.

DeMets, C., R. G. Gordon, and D. F. Argus (2010), Geologically current plate motions, *Geophys. J. Int.*, *181*, 1–80.

Dougherty, S. L., and R. W. Clayton (2014), Seismicity and structure in central Mexico: Evidence for a possible slab tear in the South Cocos plate, *J. Geophys. Res. Solid Earth*, *119*, 3424–3447, doi:10.1002/2013JB010883.

Ducea, M. N., G. E. Gehrels, S. Shoemaker, J. Ruiz, and V. A. Valencia (2004), Geologic evolution of the Xolapa Complex, southern Mexico: Evidence from U-Pb zircon geochronology, *Geol. Soc. Am. Bull.*, *116*, 1016–1025.

Espurt, N., F. Funiciello, J. Martinod, B. Guillaume, V. Regard, C. Faccenna, and S. Brusset (2008), Flat subduction dynamics and deformation of the South American plate: Insights from analog modeling, *Tectonics*, *27*, TC3011, doi:10.1029/2007TC002175.

Faccenna, C., T. W. Becker, M. S. Miller, E. Serpelloni, and S. D. Willett (2014), Isostasy, dynamic topography, and the elevation of the Apennines of Italy, *Earth Planet. Sci. Lett.*, *407*, 163–174.

Ferrari, L. (2004), Slab detachment control on mafic volcanic pulse and mantle heterogeneity in central Mexico, *Geology*, *32*, 77–80.

Ferrari, L., M. López-Martínez, G. Aguirre-Díaz, and G. Carrasco-Núñez (1999), Space-time patterns of cenozoic arc volcanism in central Mexico: From the Sierra Madre Occidental to the Mexican Volcanic Belt, *Geology*, *27*, 303–306.

Ferrari, L., T. Orozco-Esquivel, V. Manea, and M. Manea (2012), The dynamic history of the Trans-Mexican Volcanic Belt and the Mexico subduction zone, *Tectonophysics*, *522*, 122–149.

Fix, J. E. (1975), The crust and upper mantle of central Mexico, *Geophys. J. Int.*, *43*, 453–499.

Flament, N., M. Gurnis, and R. D. Müller (2013), A review of observations and models of dynamic topography, *Lithosphere*, *5*, 189–210.

Funiciello, F., C. Faccenna, A. Heuret, E. Di Giuseppe, S. Lallemand, and T. W. Becker (2008), Trench migration, net rotation and slab-mantle coupling, *Earth Planet. Sci. Lett.*, *271*, 233–240.

Gérault, M., T. W. Becker, B. J. P. Kaus, C. Faccenna, L. N. Moresi, and L. Husson (2012), The role of slabs and oceanic plate geometry for the net rotation of the lithosphere, trench motions, and slab return flow, *Geochem. Geophys. Geosyst.*, *13*, Q04001, doi:10.1029/2011GC003934.

Ghosh, A., T. W. Becker, and E. D. Humphreys (2013), Dynamics of the North American continent, *Geophys. J. Int.*, *194*, 651–669.

Gómez-Tuena, A., M. T. Orozco-Esquivel, and L. Ferrari (2007), Igneous petrogenesis of the Trans-Mexican Volcanic Belt, in *SPE422: Geology of México: Celebrating the Centenary of the Geological Society of México*, pp. 129–181, Geol. Soc. Am., Boulder, Colo.

Guillaume, B., J. Martinod, L. Husson, M. Roddaz, and R. Riquelme (2009), Neogene uplift of central eastern Patagonia: Dynamic response to active spreading ridge subduction?, *Tectonics*, *28*, TC2009, doi:10.1029/2008TC002324.

Guillaume, B., M. Moroni, F. Funiciello, C. Faccenna, and J. Martinod (2010), Mantle flow and dynamic topography associated with slab window opening: Insights from laboratory models, *Tectonophysics*, *496*, 83–98.

Gurnis, M. (1990), Bounds on global dynamic topography from Phanerozoic flooding of continental platforms, *Nature*, *344*, 754–756.

Gurnis, M. (1993), Phanerozoic marine inundation of continents driven by dynamic topography above subducting slabs, *Nature*, *364*, 589–593.
Gutscher, M.-A., W. Spakman, H. Bijwaard, and E. R. Engdahl (2000), Geodynamics of flat subduction: Seismicity and tomographic constraints from the Andean margin, *Tectonics*, *19*, 814–833.
Holt, A. F., T. W. Becker, and B. A. Buffet (2015), Trench migration and overriding plate stress in dynamic subduction models, *Geophys. J. Int.*, *201*(1), 172–192.
Humphreys, E. D., and D. Coblentz (2007), North American dynamics and western U.S. tectonics, *Rev. Geophys.*, *45*, RG3001, doi:10.1029/2005RG000181.
Husker, A., and P. M. Davis (2009), Tomography and thermal state of the Cocos plate subduction beneath Mexico City, *J. Geophys. Res.*, *114*, B04306, doi:10.1029/2008JB006039.
Husson, L. (2006), Dynamic topography above retreating subduction zones, *Geology*, *34*, 741–744.
Husson, L., B. Guillaume, F. Funiciello, C. Faccenna, and L. H. Royden (2012), Unraveling topography around subduction zones from laboratory models, *Tectonophysics*, *526*, 5–15.
Husson, L., M. Bernet, S. Guillot, P. Huyghe, J.-L. Mugnier, A. Replumaz, X. Robert, and P. Van der Beek (2014), Dynamic ups and downs of the Himalaya, *Geology*, *42*, 839–842.
Iglesias, A., R. Clayton, X. Pérez-Campos, S. Singh, J. Pacheco, D. García, and C. Valdés-González (2010), S wave velocity structure below central Mexico using high-resolution surface wave tomography, *J. Geophys. Res.*, *115*, B06307, doi:10.1029/2009JB006332.
Isacks, B., and M. Barazangi (1977), Geometry of Benioff zones: lateral segmentations and downward bending of subducted lithosphere, in *Island Arcs, Deep Sea Trenches, and Back-Arc Basins, Maurice Ewing*, vol. 1, edited by M. Talwani and W. C. Pitman III, pp. 99–114, AGU, Washington, D. C.
Jordán, T. E., B. L. Isacks, R. W. Allmendinger, J. A. Brewer, V. A. Ramos, and C. J. Ando (1983), Andean tectonics related to geometry of subducted Nazca plate, *Geol. Soc. Am. Bull.*, *94*, 341–361.
Kaban, M. K., A. G. Petrunin, H. Schmeling, and M. Shahraki (2014), Effect of decoupling of lithospheric plates on the observed geoid, *Surv. Geophys.*, *35*, 1361–1373, doi:10.1007/s10712-014-9281-3.
Kim, Y., R. W. Clayton, and J. M. Jackson (2010), Geometry and seismic properties of the subducting Cocos plate in central Mexico, *J. Geophys. Res.*, *115*, B06310, doi:10.1029/2009JB006942.
Kim, Y., M. S. Miller, F. Pearce, and R. W. Clayton (2012a), Seismic imaging of the Cocos plate subduction zone system in central Mexico, *Geochem. Geophys. Geosyst.*, *13*, Q07001, doi:10.1029/2012GC004033.
Kim, Y., R. W. Clayton, and J. M. Jackson (2012b), Distribution of hydrous minerals in the subduction system beneath Mexico, *Earth Planet. Sci. Lett.*, *341*, 58–67.
Kim, Y., R. W. Clayton, P. D. Asimow, and J. M. Jackson (2013), Generation of talc in the mantle wedge and its role in subduction dynamics in central Mexico, *Earth Planet. Sci. Lett.*, *384*, 81–87.
Kostoglodov, V., A. Husker, N. M. Shapiro, J. S. Payero, M. Campillo, N. Cotte, and R. Clayton (2010), The 2006 slow slip event and nonvolcanic tremor in the Mexican subduction zone, *Geophys. Res. Lett.*, *37*, L24301, doi:10.1029/2010GL045424.
Krien, Y., and L. Fleitout (2008), Gravity above subduction zones and forces controlling plate motions, *J. Geophys. Res.*, *113*, B09407, doi:10.1029/2007JB005270.
Lachenbruch, A. H., and P. Morgan (1990), Continental extension, magmatism and elevation; formal relations and rules of thumb, *Tectonophysics*, *174*, 39–62.
Lithgow-Bertelloni, C., and M. Gurnis (1997), Cenozoic subsidence and uplift of continents from time-varying dynamic topography, *Geophys. Res. Lett.*, *25*, 735–738.
Liu, S., D. Nummedal, and L. Liu (2011), Migration of dynamic subsidence across the Late Cretaceous United States Western Interior Basin in response to Farallon plate subduction, *Geology*, *39*, 555–558.
Manea, V., and M. Gurnis (2007), Subduction zone evolution and low viscosity wedges and channels, *Earth Planet. Sci. Lett.*, *264*, 22–45.
Manea, V. C., M. Manea, and L. Ferrari (2013), A geodynamical perspective on the subduction of Cocos and Rivera plates beneath Mexico and Central America, *Tectonophysics*, *609*, 56–81.
Márquez, A., R. Oyarzun, M. Doblas, and S. P. Verma (1999), Alkalic (ocean-island basalt type) and calc-alkalic volcanism in the Mexican Volcanic Belt: A case for plume-related magmatism and propagating rifting at an active margin?, *Geology*, *27*, 51–54.
Mitrovica, J. X., C. Beaumont, and G. T. Jarvis (1989), Tilting of continental interiors by the dynamical effects of subduction, *Tectonics*, *8*, 1079–1094.
Molina-Garza, R., and J. Urrutia-Fucugauchi (1993), Deep crustal structure of central Mexico derived from interpretation of bouguer gravity anomaly data, *J. Geodyn.*, *17*, 181–201.
Morán-Zenteno, D. J., P. Corona-Chavez, and G. Tolson (1996), Uplift and subduction erosion in southwestern Mexico since the Oligocene: Pluton geobarometry constraints, *Earth Planet. Sci. Lett.*, *141*, 51–65.
Müller, R. D., M. Sdrolias, C. Gaina, and W. R. Roest (2008), Age, spreading rates and spreading asymmetry of the world's ocean crust, *Geochem. Geophys. Geosyst.*, *9*, Q04006, doi:10.1029/2007GC001743.
Nishenko, S., and S. Singh (1987), Conditional probabilities for the recurrence of large and great interplate earthquakes along the Mexican subduction zone, *Bull. Seismol. Soc. Am.*, *77*, 2095–2114.
O'Driscoll, L. J., E. D. Humphreys, and F. Saucier (2009), Subduction adjacent to deep continental roots: Enhanced negative pressure in the mantle wedge, mountain building and continental motion, *Earth Planet. Sci. Lett.*, *280*, 61–70.
O'Driscoll, L. J., M. A. Richards, and E. D. Humphreys (2012), Nazca-South America interactions and the late Eocene-late Oligocene flat-slab episode in the Central Andes, *Tectonics*, *31*, TC2013, doi:10.1029/2011TC003036.
Orozco-Esquivel, T., C. M Petrone, L. Ferrari, T. Tagami, and P. Manetti (2007), Geochemical and isotopic variability in lavas from the Eastern Trans-Mexican Volcanic Belt: Slab detachment in a subduction zone with varying dip, *Lithos*, *93*, 149–174.
Payero, J. S., V. Kostoglodov, N. Shapiro, T. Mikumo, A. Iglesias, X. Pérez-Campos, and R. W. Clayton (2008), Nonvolcanic tremor observed in the Mexican subduction zone, *Geophys. Res. Lett.*, *35*, L07305, doi:10.1029/2007GL032877.
Pérez-Campos, X., Y. Kim, A. Husker, P. M. Davis, R. W. Clayton, A. Iglesias, J. F. Pacheco, S. K. Singh, V. C. Manea, and M. Gurnis (2008), Horizontal subduction and truncation of the Cocos plate beneath central Mexico, *Geophys. Res. Lett.*, *35*, L18303, doi:10.1029/2008GL035127.
Piromallo, P., T. W. Becker, F. Funiciello, and C. Faccenna (2006), Three-dimensional instantaneous mantle flow induced by subduction, *Geophys. Res. Lett.*, *33*, L08304, doi:10.1029/2005GL025390.
Radiguet, M., F. Cotton, M. Vergnolle, M. Campillo, A. Walpersdorf, N. Cotte, and V. Kostoglodov (2012), Slow slip events and strain accumulation in the Guerrero gap, Mexico, *J. Geophys. Res.*, *117*, B04305, doi:10.1029/2011JB008801.

Singh, S., L. Astiz, and J. Havskov (1981), Seismic gaps and recurrence periods of large earthquakes along the Mexican subduction zone: A reexamination, *Bull. Seismol. Soc. Am.*, *71*, 827–843.
Singh, S. K., and M. Pardo (1993), Geometry of the Benioff Zone and state of stress in the overriding plate in central Mexico, *Geophys. Res. Lett.*, *20*, 1483–1486.
Skinner, S. M., and R. W. Clayton (2011), An evaluation of proposed mechanisms of slab flattening in central Mexico, *Pure Appl. Geophys.*, *168*, 1461–1474.
Song, T.-R. A., and Y. Kim (2012), Localized seismic anisotropy associated with long-term slow-slip events beneath southern Mexico, *Geophys. Res. Lett.*, *39*, L09308, doi:10.1029/2012GL051324.
Song, T.-R. A., D. V. Helmberger, M. R. Brudzinski, R. W. Clayton, P. Davis, X. Pérez-Campos, and S. K. Singh (2009), Subducting slab ultra-slow velocity layer coincident with silent earthquakes in southern Mexico, *Science*, *324*, 502–506.
Spencer, J. E. (1996), Uplift of the Colorado Plateau due to lithosphere attenuation during Laramide low-angle subduction, *J. Geophys. Res.*, *101*, 13,595–13,609.
Stadler, G., M. Gurnis, C. Burstedde, L. C. Wilcox, L. Alisic, and O. Ghattas (2010), The dynamics of plate tectonics and mantle flow: From local to global scales, *Science*, *329*, 1033–1038.
Stegman, D. R., R. Farrington, F. A. Capitanio, and W. P. Schellart (2010), A regime diagram for subduction styles from 3-D numerical models of free subduction, *Tectonophysics*, *483*, 29–45.
Steinberger, B. (2007), Effects of latent heat release at phase boundaries on flow in the Earth's mantle, phase boundary topography and dynamic topography at the Earth's surface, *Phys. Earth Planet. Inter.*, *164*, 2–20.
Stubailo, I., C. Beghein, and P. Davis (2012), Structure and anisotropy of the Mexico subduction zone based on Rayleigh-wave analysis and implications for the geometry of the Trans-Mexican Volcanic Belt, *J. Geophys. Res.*, *117*, B05303, doi:10.1029/2011JB008631.
Suárez, G., T. Monfret, G. Wittlinger, and C. David (1990), Geometry of subduction and depth of the seismogenic zone in the Guerrero gap, Mexico, *Nature*, *345*, 336–338.
Suter, M., M. L. Martínez, O. Q. Legorreta, and M. C. Martínez (2001), Quaternary intra-arc extension in the central Trans-Mexican Volcanic Belt, *Geol. Soc. Am. Bull.*, *113*, 693–703.
Turcotte, D. L., and G. Schubert (2002), *Geodynamics*, 2nd ed., Cambridge Univ. Press, Cambridge, U. K.
Urrutia-Fucugauchi, J., and J. H. Flores-Ruiz (1996), Bouguer gravity anomalies and regional crustal structure in central Mexico, *Int. Geol. Rev.*, *38*, 176–194.
Weber, R. M., P. J. Wallace, and A. D. Johnston (2012), Experimental insights into the formation of high-Mg basaltic andesites in the Trans-Mexican Volcanic Belt, *Contrib. Mineral. Petrol.*, *163*, 825–840.
Wessel, P., W. H. Smith, R. Scharroo, J. Luis, and F. Wobbe (2013), Generic Mapping Tools: Improved version released, *Eos Trans. AGU*, *94*, 409–410, doi:10.1002/2013EO450001.
Wiens, D. A., J. A. Conder, and U. H. Faul (2008), The seismic structure and dynamics of the mantle wedge, *Annu. Rev. Earth Planet. Sci.*, *36*, 421–455.
Zhang, N., S. Zhong, and R. M. Flowers (2012), Predicting and testing continental vertical motion histories since the paleozoic, *Earth Planet. Sci. Lett.*, *317*, 426–435.
Zhong, S., and G. F. Davies (1999), Effects of plate and slab viscosities on geoid, *Earth Planet. Sci. Lett.*, *170*, 487–496.
Zhong, S., and M. Gurnis (1994), Controls on trench topography from dynamic models of subducted slabs, *J. Geophys. Res.*, *99*, 15,683–15,695.